ELSEVIER

Modeling of water transport through the membrane electrode assembly for direct methanol fuel cells

C. Xu, T.S. Zhao*, W.W. Yang

*Department of Mechanical Engineering, The Hong Kong University of Science and Technology,
Clear Water Bay, Kowloon, Hong Kong SAR, China*

Abstract

In this work, a one-dimensional, isothermal two-phase mass transport model is developed to investigate the water transport through the membrane electrode assembly (MEA) for liquid-feed direct methanol fuel cells (DMFCs). The liquid (methanol–water solution) and gas (carbon dioxide gas, methanol vapor and water vapor) two-phase mass transport in the porous anode and cathode is formulated based on classical multiphase flow theory in porous media. In the anode and cathode catalyst layers, the simultaneous three-phase (liquid and vapor in pores as well as dissolved phase in the electrolyte) water transport is considered and the phase exchange of water is modeled with finite-rate interfacial exchanges between different phases. This model enables quantification of the water flux corresponding to each of the three water transport mechanisms through the membrane for DMFCs, such as diffusion, electro-osmotic drag, and convection. Hence, with this model, the effects of MEA design parameters on water crossover and cell performance under various operating conditions can be numerically investigated.
© 2007 Elsevier B.V. All rights reserved.

Keywords: Direct methanol fuel cell (DMFC); Two-phase mass transport model; Water crossover; Water transport; Water management

1. Introduction

The liquid-feed direct methanol fuel cell (DMFC) has recently received much attention as it has been regarded as an attractive alternative to conventional power sources for portable electronic devices. However, the commercialization of DMFC technology is still hindered by several technological problems, among which water management is one of the key issues [1–4]. Unlike in gas-hydrogen-feed polymer electrolyte fuel cells (PEFCs), in DMFCs, liquid methanol solution is fed to its anode. As a result, liquid water is prone to transport through the membrane from the anode to the cathode, which is usually called water crossover. Water crossover can not only result in a water loss from the anode, but also increase the difficulty in avoiding the cathode-flooding problem, downgrading the DMFC performance significantly. Therefore, suppressing water crossover is beneficial not only for simplifying the DMFC system but also for improving cell performance. To this end, it is essential to gain a better understanding of the mechanisms of

water crossover in DMFCs, which appears to be significantly different with that in PEFCs [1–3]. Over the past decade, the problem of water crossover through Nafion membranes for DMFCs has been experimentally studied extensively [1–11]. However, it is rather difficult to shed light on each mechanism of water crossover through the membrane through experimental investigations, as water transport in DMFCs is intrinsically coupled with a series of physicochemical processes, including species transport, momentum transport, and multiple electrochemical reactions. Hence, mathematical modeling plays an important role, as it can provide a powerful and economical tool to quantify the complex transport processes and thus elucidate the water transport mechanisms in DMFCs.

Recently, extensive efforts have been made to develop two-phase mass transport models for DMFCs [12–17], which are more realistic and effective as the coexisting liquid and gas flow behavior has a significant influence on the mass transport processes [18,19]. Murgia et al. [12] presented a one-dimensional model based on phenomenological transport equations for DMFCs. In order to consider the two-phase flow interaction in the diffusion layer (DL), they introduced a Gaussian function to approximately account for the influence of the

---

Nomenclature

a_w	water vapor activity
A_{lg}	interfacial specific area between liquid and gas phase ($m^2\,m^{-3}$)
A_v	specific area ($m^2\,m^{-3}$)
C	molar concentration ($mol\,m^{-3}$)
D	diffusivity ($m^2\,s^{-1}$)
F	Faraday constant ($96,478\,C\,mol^{-1}$)
h_{lg}	interfacial transfer rate constant for methanol ($m\,s^{-1}$)
I	current density ($A\,m^{-2}$)
I_p	parasitic current resulting from methanol crossover ($A\,m^{-2}$)
j_0	exchange current density ($A\,m^{-2}$)
j_a	anode current density ($A\,m^{-3}$)
j_c	cathode current density ($A\,m^{-3}$)
k_c	condensation rate (s^{-1})
k_e	evaporation rate ($atm\,s$)$^{-1}$
k_r	relative permeability
K	permeability of porous material (m^2)
$\dot{m}$	Source term in mass conservation equation ($kg\,m^{-3}\,s^{-1}$)
M	molecular weight ($kg\,mol^{-1}$)
n_d	electro-osmotic drag coefficient
N	mol flux ($mol\,m^{-2}\,s^{-1}$), or Nafion
p_c	capillary pressure (Pa)
p_g	gas phase pressure (Pa)
p_l	liquid phase pressure (Pa)
R	gas constant, $J\,(mol\,K)^{-1}$
$\dot{R}$	source term in species conservation equation ($mol\,m^{-3}\,s^{-1}$)
$\tilde{R}$	interfacial species transfer rate ($mol\,m^{-3}\,s^{-1}$)
$R_{contact}$	ohmic contact resistance ($\Omega\,m^2$)
s	liquid saturation
T	temperature (K)
V_0	thermodynamic equilibrium voltage (V)
V_{cell}	Cell voltage (V)
x	coordinate, m, or mole fraction in liquid solution
y	Coordinate, m, or mole fraction in gas mixture

Greek letters

α	net water-transport coefficient
α_a	anode transfer coefficient at anode
α_c	cathode transfer coefficient at cathode
δ	thickness of porous layer (m)
ε	porosity of porous medium
γ	reaction order of ORR
η	overpotential (V)
κ	ionic conductivity of membrane ($\Omega^{-1}\,m^{-1}$)
$\kappa_a(\kappa_d)$	absorption (desorption) coefficient (s^{-1})
$\kappa_{ads}(\kappa_{des})$	H_2O^{dis} absorption (H_2O^{liq} desorption) coefficient (s^{-1})
λ	water content
μ	viscosity ($kg\,m^{-1}\,s^{-1}$)
θ	contact angle ($°$)
ρ	density ($kg\,m^{-3}$)
σ	interfacial tension ($N\,m^{-1}$)

Superscripts

eff	effective value
in	inlet condition
ref	reference value
sat	saturated value
*	in equilibrium

Subscripts

a	anode
bf	back flow
c	cathode, or capillary
dry	dry membrane
dv	from dissolved phase to vapor phase
e	electrolyte, or evaporation
g	gas phase
l	liquid phase
ld	from liquid phase to dissolved phase
mem	membrane
M	methanol
MV	methanol vapor
rg	relative value for gas phase
rl	relative value for liquid phase
vapor	water vapor
vl	from vapor phase to liquid phase
W	water
we	dissolved water
WV	water vapor

capillary pressure on the effective gas porosity. Wang and Wang [13] modeled a DMFC using the multiphase mixture model, in which the species in the liquid and gas phase are assumed to be at the thermodynamic equilibrium condition. Rice and Faghri [14] proposed a transient, multiphase model for a passive fuel feed DMFC. Noteworthy is that the evaporation/condensation of methanol and water was formulated in a manner to capture non-equilibrium effects between phases, which differed from the thermodynamic equilibrium assumption employed elsewhere [12,13]. Most recently, Yang and Zhao [16,17] developed a two-phase mass transport model for liquid-feed DMFCs, which was formulated based on classical multiphase flow theory in porous medium and with the effect of non-equilibrium evaporation and condensation of methanol and water taken account. Most of previous work about DMFCs mainly investigated the transport phenomena in porous regions of the anode and the cathode, but relatively little efforts have been made on modeling of the simultaneous water transport across the membrane.

Water transport across the Nafion membrane has been extensively modeled over the past decade for hydrogen-feed PEFCs [20–38]. Springer et al. [20] developed a simple, one-dimensional isothermal model of a complete PEFC that has

provided useful insight into the cell's water transport mechanism. They considered gas transport in the electrode and dissolved water transport in the membrane, and applied thermodynamics phase equilibrium condition between dissolved water in the membrane and water vapor in the electrode at the membrane/electrode interfaces. This equilibrium assumption has been widely adopted by many researchers [21–29] in modeling the water transport through the membrane. This model had been extended by Kulikovsky [30], who considered transport of both gas phase and dissolved water in electrolyte phase in the catalyst layers (CLs). They also assumed that, in the CLs, the dissolved water phase is in phase equilibrium with the water vapor in voids, and thus water transport in the CLs can be dealt with based on the "fictitious water concentration" treatment. This approach can also be found elsewhere [25–28]. However, the equilibrium assumption between water vapor and dissolved water, albeit suitable as an approximation, is not strictly correct, since the equilibrium state is not achieved instantly but over a prolonged period of time [31]. As thus, Siegel et al. [32] and Vorobev et al. [31] developed models for PEFCs, in which they did not assume equilibrium between water vapor and dissolved water in the CLs, but rather considered them as different phases exchanging at a finite rate. Most recently, since under typical PEFC operating conditions both liquid water and water vapor exists in voids of the electrodes, a more realistic one-dimensional model had been developed by Shah et al. [33,34], in which three phases of water (i.e., dissolved water in the electrolyte, water vapor in voids and liquid water in voids) were considered. Notably, the equilibrium assumption between different phases was not employed, and evaporation and condensation between liquid and vapor, as well as adsorption and desorption between dissolved water and vapor and between dissolved water and liquid, were introduced for the finite-rate interfacial mass transport. This basic feature of the model enables in capturing the convoluted water transport phenomena across the whole MEA for PEFCs.

However, with regard to DMFCs, most of previous models assumed that the membrane was fully hydrated and no water diffusion occurred, and little work about the water transport across the membrane was reported [15,39–44]. Meyers and Newman [39–41] developed a mathematical model that described the transport of species in a multi-component membrane. Liquid phase in the anode and gas phase in the cathode were considered, and the equilibrium condition was assumed between the membrane and the adjacent liquid or vapor phases. Similarly, Schultz and Sundmacher [42] developed a one-dimensional rigorous process model for a single-cell DMFC, which also introduced phase equilibrium assumption between the dissolved water and the water inside the pores of both CLs. These two reports all considered single phase flow in both the anode and the cathode, which were just for a first approximation and could not reflect the mass transport processes in real liquid–gas two-phase flow occurring in the DMFC. Recently, Liu and Wang [15,43] developed a liquid–gas two-phase transport model for DMFCs, in which the water-crossover flux was determined based on the conditions at the CL/membrane interfaces and the phase equilibrium assumption. Different water-crossover mechanisms, including diffusion, electro-osmotic drag and convection, were analyzed.

The objective of this work is to develop a one-dimensional, isothermal two-phase mass transport model for liquid-feed DMFCs. Water transport in three phases (i.e., liquid, vapor, and dissolved phase) is considered simultaneously, and finite-rate interfacial exchanges between different phases are introduced without any phase equilibrium assumptions. With these finite-rate interfacial exchanges between different phases, dissolved water transport across the membrane can be intrinsically coupled with the liquid–gas two-phase flow in the porous regions of both the anode and the cathode. Thus, this model enables us to investigate different water-crossover mechanisms separately, and study the effect of cell operating conditions on water crossover. Furthermore, since the cathode porous region, especially the cathode micro-porous layer (MPL), plays an important role in both water crossover through the membrane and water ejection from the cathode [1,2,45–47], this model also includes MPLs between the DL and CL of both the anode and the cathode, which enables us to study the effect of membrane electrode assembly (MEA) structure on water transport in the DMFC. The results presented in this work provide a useful insight into the water-crossover mechanisms, which is helpful for the optimal design of the MEA to reduce water crossover and to achieve better cell performance.

2. Formulation

We consider a MEA, as illustrated in Fig. 1, which consists of seven layers from the interface I between the anode channel and anode diffusion layer (ADL) to the interface VIII between the cathode diffusion layer (CDL) and cathode gas channel. Note that micro-porous layers (MPLs) are also included between the catalyst layers (CLs) and coarse DLs at both the anode and the cathode. At the anode, liquid methanol solution is fed from the channel through the DL to the CL, while the produced gas CO_2 is expelled from the DL to the channel. Thus, a liquid–gas two-phase counter flow is involved in the anode porous region,
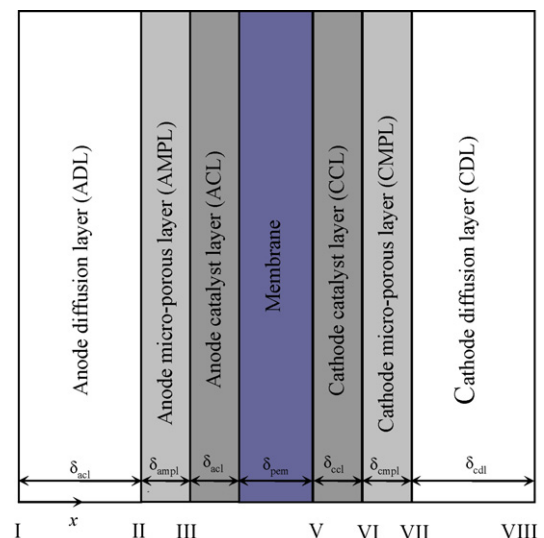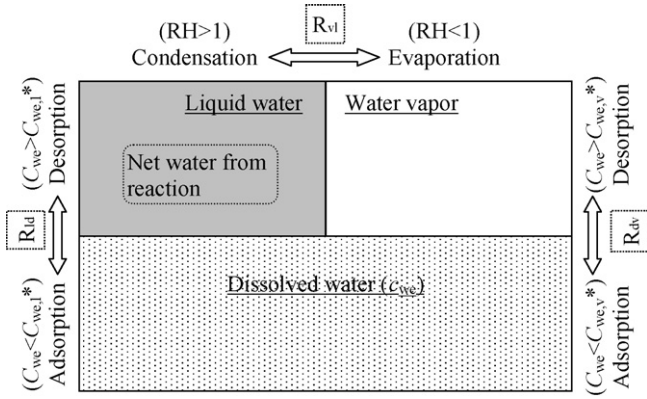

Fig. 1. Schematic of the model domain.

Fig. 2. Schematic representation of the interaction between water in the three phases in the catalyst layers.

including the ADL, the AMPL and the ACL. Similarly, in the gas-feed cathode, liquid water usually resides in the porous region under typical operating conditions, and thus a liquid–gas two-phase counter flow also occurs. In the following, we present a one-dimensional mass transport model for water through the MEA.

2.1. Phase changes of water in the CLs

In the CLs, both liquid and water vapor can dissolve in the electrolyte (typically Nafion) with the effect of adsorption to form dissolved water. Thus, as schematically illustrated in Fig. 2, water exists in three phases in the CLs: liquid, vapor, and the dissolved phase. To model the water transport in the CLs, the phase-change rates between different phases are needed. As shown in Fig. 2, both the water produced at the cathode and that consumed at the anode is in the liquid phase. For the phase change between liquid and vapor, the rate of condensation and evaporation can be modeled using the finite-rate approach [17]:

$$\tilde{R}_{\mathrm{vl}} = h_{\mathrm{vl}}(x_{\mathrm{vapor}} p_{\mathrm{g}} - p_{\mathrm{vapor}}^{\mathrm{sat}}) \tag{1}$$

where $p_{\mathrm{vapor}}^{\mathrm{sat}}$ is the saturation pressure of water vapor, p_{g} is the gas pressure, and x_{vapor} is the molar fraction of water vapor in the gas phase. Eq. (1) indicates that the phase change between liquid and vapor is driven by the deviation of the local thermodynamic state from equilibrium. Note that the driving force $(x_{\mathrm{vapor}} p_{\mathrm{g}} - p_{\mathrm{vapor}}^{\mathrm{sat}})$ is positive for condensation but negative for evaporation. The mass-transfer coefficient h_{vl} can be given by [17,33]:

$$h_{\mathrm{vl}} = \frac{k_{\mathrm{c}} \varepsilon (1-s) x_{\mathrm{vapor}}}{2RT} \left(1 + \frac{|x_{\mathrm{vapor}} p_{\mathrm{g}} - p_{\mathrm{vapor}}^{\mathrm{sat}}|}{x_{\mathrm{vapor}} p_{\mathrm{g}} - p_{\mathrm{vapor}}^{\mathrm{sat}}} \right)$$
$$+ \frac{k_{\mathrm{e}} \varepsilon s \rho_{\mathrm{l}}}{2M_{\mathrm{H_2O}}} \left(1 - \frac{|x_{\mathrm{vapor}} p_{\mathrm{g}} - p_{\mathrm{vapor}}^{\mathrm{sat}}|}{x_{\mathrm{vapor}} p_{\mathrm{g}} - p_{\mathrm{vapor}}^{\mathrm{sat}}} \right) \tag{2}$$

where k_{c} and k_{e} are the condensation and evaporation rate constants, ε the porosity of the porous region, s the liquid water saturation, T the cell temperature, ρ_{l} the density of liquid and $M_{\mathrm{H_2O}}$ the molecular weight of water. In the above expression, a sufficiently high values of k_{c} and k_{e} are chosen so that the vapor is essentially in equilibrium with the liquid.

In a similar fashion, the dissolved water-vapor transfer rate through desorption and adsorption can be expressed as:

$$\tilde{R}_{\mathrm{dv}} = h_{\mathrm{dv}}(C_{\mathrm{we}} - C_{\mathrm{we,v}}^{*}) \tag{3}$$

where C_{we} is the dissolved water concentration in the electrolyte and $C_{\mathrm{we,v}}^{*}$ is the equilibrium dissolved concentration when the polymer is in equilibrium with water-vapor-saturated gas. The driving force $(C_{\mathrm{we}} - C_{\mathrm{we,v}}^{*})$ is positive for desorption but negative for adsorption. The dissolved water concentration C_{we} can be transformed to the water content λ in the electrolyte and the relationship between C_{we} and λ is given by

$$\lambda = \frac{EW}{\rho_{\mathrm{dry}}} C_{\mathrm{we}} \tag{4}$$

In Eq. (3), $C_{\mathrm{we,v}}^{*}$ can be derived from the equilibrium water content $\lambda_{\mathrm{we,v}}^{*}$ at 353 K [48] to give

$$\lambda_{\mathrm{we,v}@353\,\mathrm{K}}^{*} = 0.3 + 10.8a_{\mathrm{w}} - 16a_{\mathrm{w}}^{2} + 14.1a_{\mathrm{w}}^{3} \tag{5}$$

and at 303 K [20]

$$\lambda_{\mathrm{we,v}@303\,\mathrm{K}}^{*} = 0.043 + 17.81a_{\mathrm{w}} - 39.85a_{\mathrm{w}}^{2} + 36.0a_{\mathrm{w}}^{3} \tag{6}$$

where a_{w} is the water vapor activity $(a_{\mathrm{w}} = x_{\mathrm{vapor}} p_{\mathrm{g}} / p_{\mathrm{vapor}}^{\mathrm{sat}})$. The equilibrium water content $\lambda_{\mathrm{we,v}}^{*}$ at any temperature can thus be approximated by [49]

$$\lambda_{\mathrm{we,v}}^{*} = \lambda_{\mathrm{we,v}@303\,\mathrm{K}}^{*} + \frac{\lambda_{\mathrm{we,v}@353\,\mathrm{K}}^{*} - \lambda_{\mathrm{we,v}@303\,\mathrm{K}}^{*}}{50}(T - 303) \tag{7}$$

The coefficients of adsorption and desorption h_{dv} can be given by [33,34]

$$h_{\mathrm{dv}} = \frac{1}{2}\kappa_{\mathrm{d}}(1-s)\lambda \left(1 + \frac{|C_{\mathrm{we}} - C_{\mathrm{we,v}}^{*}|}{C_{\mathrm{we}} - C_{\mathrm{we,v}}^{*}} \right)$$
$$+ \frac{1}{2}\kappa_{\mathrm{a}}(1-s)\lambda \left(1 - \frac{|C_{\mathrm{we}} - C_{\mathrm{we,v}}^{*}|}{C_{\mathrm{we}} - C_{\mathrm{we,v}}^{*}} \right) \tag{8}$$

where κ_{d} and κ_{a} are the desorption and adsorption rate constants.

It is known that when the electrolyte Nafion is submerged in liquid water its equilibrium water content appears to jump discontinuously to a higher value of $\lambda_{\mathrm{we,l}}^{*} = 22$ [34,39–41]. To capture this anomaly we also introduce the liquid-dissolved transfer rate through desorption and adsorption, which is driven by the deviation of the water concentration from the equilibrium one and is given by

$$\tilde{R}_{\mathrm{ld}} = h_{\mathrm{ld}}(C_{\mathrm{we,l}}^{*} - C_{\mathrm{we}}) \tag{9}$$

where $C_{\mathrm{we,l}}^{*}$ is the equilibrium dissolved concentration when the electrolyte is in equilibrium with liquid water. The driving force $(C_{\mathrm{we,l}}^{*} - C_{\mathrm{we}})$ is positive for desorption of water from the electrolyte to form liquid but negative for adsorption of liquid water to the electrolyte in the CLs. The coefficients of adsorption and desorption h_{ld} is assumed to be dependent of liquid saturation

and can be given by [33,34]

$$
\begin{aligned}
h_{\mathrm{ld}} &= \frac{1}{2}\kappa_{\mathrm{ads}}s\left(1 - \frac{|C_{\mathrm{we}} - C^*_{\mathrm{we,1}}|}{C_{\mathrm{we}} - C^*_{\mathrm{we,1}}}\right) \\
&+ \frac{1}{2}\kappa_{\mathrm{des}}s\left(1 + \frac{|C_{\mathrm{we}} - C^*_{\mathrm{we,1}}|}{C_{\mathrm{we}} - C^*_{\mathrm{we,1}}}\right)
\end{aligned}
\tag{10}
$$

where κ_{des} and κ_{ads} are the desorption and adsorption rate constants between liquid and dissolved water. The values of κ_{des} and κ_{ads} are chosen large enough to avoid significant overshoot of c_{we} when it exceeds $C^*_{\mathrm{we,1}}$. These parameters and their values are given in Table 1.

2.2. Governing equations for mass transport

We now present the governing equations for the one-dimensional, steady-state, isothermal two-phase mass transport in the porous regions of the DMFC anode and cathode, as well as for the dissolved water transport in the electrolyte in both the CLs and the membrane. The details of the two-phase mass transport model in the porous regions can be found elsewhere [16,17]. Referring to Fig. 1, in the anode and cathode porous regions (from Interface I to IV and from V to VIII), there are a total of nine variables that are used to describe mass transport of each species, including the concentration of liquid methanol ($C_{\mathrm{M,l}}$), the concentration of methanol vapor ($C_{\mathrm{MV,g}}$), gas pressure in the anode ($p_{\mathrm{g,a}}$), liquid pressure in the anode ($p_{\mathrm{l,a}}$), the concentration of water vapor in the anode ($C_{\mathrm{WV,g,a}}$), the concentration of gas oxygen in the cathode ($C_{\mathrm{O_2,g}}$), liquid phase pressure in the cathode ($p_{\mathrm{l,c}}$), gas phase pressure in the cathode ($p_{\mathrm{g,c}}$) and the concentration of water vapor in the cathode ($C_{\mathrm{WV,g,c}}$). In the electrolyte region (from III to VI), variable of dissolved water concentration in the electrolyte (C_{we}) are involved. The governing equations that describe the mass conservation of each species at different phases are given below:

Anode porous region (I–IV):

$$
p_{\mathrm{l,a}}: \quad \nabla \cdot \left(-\frac{Kk_{\mathrm{rl}}}{\mu_{\mathrm{l}}/\rho_{\mathrm{l}}}\nabla p_{\mathrm{l,a}}\right) = \dot{m}_{\mathrm{l,a}}
\tag{11}
$$

$$
p_{\mathrm{g,a}}: \quad \nabla \cdot \left(-\frac{Kk_{\mathrm{rg}}}{\mu_{\mathrm{g}}/\rho_{\mathrm{g}}}\nabla p_{\mathrm{g,a}}\right) = \dot{m}_{\mathrm{g,a}}
\tag{12}
$$

$$
C_{\mathrm{M,l}}: \quad \nabla \cdot \left[\left(-\frac{Kk_{\mathrm{rl}}}{\mu_{\mathrm{l}}}\nabla p_{\mathrm{l,a}}\right)C_{\mathrm{M,l}} - D_{\mathrm{M}}^{\mathrm{eff}}\nabla C_{\mathrm{M,l}}\right] = \dot{R}_{\mathrm{M,l,a}}
\tag{13}
$$

$$
C_{\mathrm{MV,g}}: \quad \nabla \cdot \left[\left(-\frac{Kk_{\mathrm{rg}}}{\mu_{\mathrm{g}}}\nabla p_{\mathrm{g,a}}\right)C_{\mathrm{MV,g}} - D_{\mathrm{MV,g}}^{\mathrm{eff}}\nabla C_{\mathrm{MV,g}}\right]
$$
$$
= \dot{R}_{\mathrm{MV,g}}
\tag{14}
$$

$$
C_{\mathrm{WV,g}}: \quad \nabla \cdot \left[\left(-\frac{Kk_{\mathrm{rg}}}{\mu_{\mathrm{g}}}\nabla p_{\mathrm{g,a}}\right)C_{\mathrm{WV,g,a}} - D_{\mathrm{WV,g}}^{\mathrm{eff}}\nabla C_{\mathrm{WV,g,a}}\right]
$$
$$
= \dot{R}_{\mathrm{WV,g,a}}
\tag{15}
$$

Cathode porous region (V–VIII):

$$
p_{\mathrm{g,c}}: \quad \nabla \cdot \left[\left(-\frac{Kk_{\mathrm{rg}}}{\mu_{\mathrm{g}}/\rho_{\mathrm{g}}}\right)\nabla p_{\mathrm{g,c}}\right] = \dot{m}_{\mathrm{g,c}}
\tag{16}
$$

$$
p_{\mathrm{l,c}}: \quad \nabla \cdot \left[\left(-\frac{Kk_{\mathrm{rl}}}{\mu_{\mathrm{l}}/\rho_{\mathrm{l}}}\right)\nabla p_{\mathrm{l,c}}\right] = \dot{m}_{\mathrm{l,c}}
\tag{17}
$$

$$
C_{\mathrm{O_2,g}}: \quad \nabla \cdot \left[\left(-\frac{Kk_{\mathrm{rg}}}{\mu_{\mathrm{g}}}\nabla p_{\mathrm{g,c}}\right)C_{\mathrm{O_2,g}} - D_{\mathrm{O_2,g}}^{\mathrm{eff}}\nabla C_{\mathrm{O_2,g}}\right]
$$
$$
= \dot{R}_{\mathrm{O_2,g}}
\tag{18}
$$

$$
C_{\mathrm{WV,g,c}}: \quad \nabla \cdot \left[\left(-\frac{Kk_{\mathrm{rg}}}{\mu_{\mathrm{g}}}\nabla p_{\mathrm{g,c}}\right)C_{\mathrm{WV,g,c}} - D_{\mathrm{WV,g}}^{\mathrm{eff}}\nabla C_{\mathrm{WV,g,c}}\right]
$$
$$
= \dot{R}_{\mathrm{WV,g,c}}
\tag{19}
$$

Here, it should be noted that the capillary pressure for the porous region is given by [16,17]:

$$
p_{\mathrm{c}} = p_{\mathrm{g}} - p_{\mathrm{l}} = \sigma\cos\theta(\varepsilon/K)^{0.5}J(s)
\tag{20}
$$

where $J(s)$ represents the widely-used Leverette function:

$$
J(s) = \begin{cases} 1.417(1-s) - 2.120(1-s)^2 + 1.263(1-s)^3 & 0 < \theta \leq 90^o \\ 1.417s - 2.120s^2 + 1.263s^3 & 90^o < \theta < 180^o \end{cases}
\tag{21}
$$

Thus, the liquid saturation for the porous regions of both the anode and the cathode can be determined from Eqs. (20) and (21) after obtaining the liquid pressure and gas pressure.

2.3. Electrolyte region (III–VI)

Unlike in the porous region, in the electrolyte region only dissolved water and methanol need to be considered, as the membrane is usually regarded as a gas insulator. Transport of dissolved water through the electrolyte generally depends on molecular diffusion, electro-osmotic drag and back convection. Accordingly, the flux of water crossover (N_{W}) can be given by [1,2]:

$$
N_{\mathrm{W}} = -\varepsilon_{\mathrm{e}}^{1.5}D_{\mathrm{we}}(\lambda)\nabla C_{\mathrm{we}} + n_{\mathrm{d,H_2O}}\frac{I}{F} - \frac{\varepsilon_{\mathrm{e}}K_{\mathrm{mem}}\rho_{\mathrm{l}}}{\mu_{\mathrm{l}}M_{\mathrm{H_2O}}}\nabla p_{\mathrm{l}}
\tag{22}
$$

Thus, the governing equation for the dissolved water concentration (C_{we}) is:

$$
\begin{aligned}
\nabla \cdot N_{\mathrm{W}} &= \nabla \cdot (-\varepsilon_{\mathrm{e}}^{1.5}D_{\mathrm{we}}(\lambda)\nabla C_{\mathrm{we}}) + \nabla \cdot \left(n_{\mathrm{d,H_2O}}\frac{I}{F}\right) \\
&= \begin{cases} \tilde{R}_{\mathrm{ld}} - \tilde{R}_{\mathrm{dv}} - \dot{R}_{\mathrm{bf}}(\mathrm{ACL}) \\ 0(\mathrm{PEM}) \\ \tilde{R}_{\mathrm{ld}} - \tilde{R}_{\mathrm{dv}} + \dot{R}_{\mathrm{bf}}(\mathrm{CCL}) \end{cases}
\end{aligned}
\tag{23}
$$

Here, we assume that the water-crossover flux due to back convection ($-\frac{\varepsilon_{\mathrm{e}}K_{\mathrm{mem}}\rho_{\mathrm{l}}}{\mu_{\mathrm{l}}M_{\mathrm{H_2O}}}\nabla p_{\mathrm{l}}$) is uniformly distributed across the CLs,

Table 1
Physicochemical properties

Parameters	Symbols	Value	Unit	Ref.
Porosity, permeability				
ADL	$\varepsilon_{adl}, K_{adl}$	$0.75, 1.0 \times 10^{-12}$	$-, m^2$	–
AMPL	$\varepsilon_{ampl}, K_{ampl}$	$0.3, 2.5 \times 10^{-13}$	$-, m^2$	[16]
ACL	$\varepsilon_{acl}, K_{acl}$	$0.3, 1.5 \times 10^{-14}$	$-, m^2$	[16]
MEM	$\varepsilon_{mem}, K_{mem}$	$0.3, 2.0 \times 10^{-18}$	$-, m^2$	[16]
CCL	$\varepsilon_{ccl}, K_{ccl}$	$0.3, 1.5 \times 10^{-14}$	$-, m^2$	[16]
CMPL	$\varepsilon_{cmpl}, K_{cmpl}$	$0.3, 2.5 \times 10^{-13}$	$-, m^2$	[16]
CDL	$\varepsilon_{cdl}, K_{cdl}$	$0.75, 1.0 \times 10^{-12}$	$-, m^2$	–
Nafion volume fraction				
ACL	$\varepsilon_{e,acl}$	0.3	–	–
CCL	$\varepsilon_{e,ccl}$	0.3	–	–
Diffusivities				
MeOH in water	$D_{M,l}$	$1.58 \times 10^{-9} e^{0.02623(T-298)}$	$m^2\,s^{-1}$	[16]
MeOH in Nafion	$D_{M,N}$	$4.9 \times 10^{-10} e^{[2436(1/333-1/T)]}$	$m^2\,s^{-1}$	[16]
Methanol vapor	$D_{M,g}$	$-6.954 \times 10^{-6} + 4.5986 \times 10^{-8}T + 9.4979 \times 10^{-11}T^2$	$m^2\,s^{-1}$	[17]
O_2 in gas	$D_{O_2,\,g}$	$1.775 \times 10^{-5} \left(\frac{T}{273.15}\right)^{1.823}$	$m^2\,s^{-1}$	[16]
Water vapor	$D_{WV,g}$	$2.56 \times 10^{-5} \left(\frac{T}{307.15}\right)^{2.334}$	$m^2\,s^{-1}$	[16]
Dissolved water in Nafion	D_{we}	$4.17 \times 10^{-8}\lambda(161e^{-\lambda} + 1)e^{-2436/T}$	$m^2\,s^{-1}$	[21]
Viscosity of gas phase	μ_g	2.03×10^{-5}	$kg\,m^{-1}\,s^{-1}$	[17]
Viscosity of liquid phase	μ_l	4.05×10^{-4}	$kg\,m^{-1}\,s^{-1}$	[16]
Electro-osmotic drag coefficients of water and methanol	n_{d,H_2O}	$\frac{2.5}{22}\lambda$	–	[24]
	$n_{d,M}$	$n_{d,H_2O}x_M$	–	–
Evaporation rate constant for water	k_e	1.0×10^3	$(atm\,s)^{-1}$	–
Condensation rate constant for water	k_c	1.0×10^6	s^{-1}	–
Interfacial transfer rate constant for methanol	h_{lg}	0.05	$m\,s^{-1}$	–
Specific interfacial area between liquid and gas	A_{lg}	10^5	m^{-1}	[17]
Water vapor adsorption (desorption) coefficient	$\kappa_a(\kappa_d)$	8.0 (0.25)	s^{-1}	–
Water liquid adsorption (desorption) coefficient	$\kappa_{ads}(\kappa_{des})$	4.0 (100.0)	s^{-1}	[34]
Proton conductivity in membrane	κ	$7.3e^{[1268(1/298-1/T)]}$	$\Omega^{-1}\,m^{-1}$	[16]
Henry law constant for methanol	$k_{H,M}$	$0.096e^{0.04511(T-273)}$	atm	[17]
The saturation pressure of water vapor	$\log_{10} p_{WV}^{sat}$	$-2.1794 + 0.02953(T-273) - 9.1837 \times 10^{-5}(T-273)^2 + 1.4454 \times 10^{-7}(T-273)^3$	atm	[17]
The saturation pressure of methanol vapor	p_{MV}^{sat}	$k_H x_{M,l}$	atm	[17]
Thermodynamic voltage	V_0	1.21	V	[16]
Transfer coefficient of anode	α_a	0.5	–	[16]
Transfer coefficient of cathode	α_c	1.0	–	[16]
Anode exchange current density	$A_{v,a}j_{0,M}^{ref}$	1.0×10^5	$A\,m^{-3}$	[16]
Cathode exchange current density	$A_{v,c}j_{0,O_2}^{ref}$	6.97×10^2	$A\,m^{-3}$	[16]
Anode reference concentration	C_M^{ref}	100	$mol\,m^{-3}$	[16]
Cathode reference concentration	$C_{O_2}^{ref}$	36.5	$mol\,m^{-3}$	[16]
Surface tension	σ	0.0644	$N\,m^{-1}$	[45]
Equivalent weight of ionomer	EW	1.1	$kg\,mol^{-1}$	[21]
Dry membrane density	ρ_{dry}	1980	$kg\,m^{-3}$	[21]

and the term

$$\dot{R}_{bf} = \frac{K_{mem}\rho_l}{\mu_l M_{H_2O}} \frac{\Delta p_{l,c\text{-}a}}{\delta_{mem}\delta_{cl}} \qquad (24)$$

is to account for the effect of back convection, where $\Delta p_{l,c-a}$ represents the liquid pressure difference between the cathode and the anode. The flux of methanol crossover ($N_{M,l}$), which depends on the effect of molecular diffusion, electro-osmotic drag and convection, can be given by:

$$N_{M,l} = -D_{M,N}\nabla C_{M,l} + n_{d,M}\frac{I}{F} - \left(\frac{K_{mem}}{\mu_l} \frac{\Delta p_{l,c\text{-}a}}{\delta_{mem}}\right) C_{M,l} \qquad (25)$$

It should be mentioned here that the model developed in this work can also be used to study the effect of methanol crossover on cell performance.

To make the above governing equations closed, some constitutive correlations and definitions are needed. These include relative permeability for both gas and liquid phases, effective dif-

Table 2
Constitutive relations

Parameters	Expressions	
Relative permeabilities	$k_{rl} = s^3$	Liquid
	$k_{rg} = (1-s)^3$	Gas
Effective diffusion coefficients of species [16,17]	$D_{i,g}^{eff} = D_{i,g} \varepsilon^{1.5}(1-s)^{1.5}$ i : O_2, WV, MV	ADL/AMPL ACL MEM
	$D_M^{eff} = \begin{cases} D_{M,l}\varepsilon^{1.5}s^{1.5} \\ \dfrac{(\varepsilon + \varepsilon_e)}{[\varepsilon/(D_{M,l}\varepsilon^{1.5}s^{1.5}) + \varepsilon_e/(D_{M,N}\varepsilon_e^{1.5})]} \\ D_{M,N} \end{cases}$	
General generation rate of mass in liquid phase	$\dot{m}_{l,a} = \begin{cases} M_{H_2O}\tilde{R}_{vl} - M_M\dot{R}_{MV,g} \\ M_{H_2O}(\tilde{R}_{vl} - \tilde{R}_{ld} + \dot{R}_{bf} - j_a/6F) - M_M(\dot{R}_{MV,g} + j_a/6F + I_p/6F\delta_{acl}) \end{cases}$	ADL/AMPL ACL
	$\dot{m}_{l,c} = \begin{cases} M_{H_2O}\tilde{R}_{vl} \\ M_{H_2O}(\tilde{R}_{vl} - \tilde{R}_{ld} - \dot{R}_{bf} + ((j_c - I_p/\delta_{ccl})/2F + I_p/3F\delta_{ccl})) \end{cases}$	CDL/CMPL CCL
General generation rate of mass in gas phase	$\dot{m}_{g,a} = \begin{cases} -M_{H_2O}\tilde{R}_{vl} + M_M\dot{R}_{MV,g} \\ M_{CO_2} j_a/6F + M_{H_2O}(\tilde{R}_{dv} - \tilde{R}_{vl}) + M_M\dot{R}_{MV,g} \end{cases}$	ADL/AMPL ACL
	$\dot{m}_{g,c} = \begin{cases} -M_{H_2O}\tilde{R}_{vl} \\ -M_{O_2} j_c/4F + M_{CO_2} I_p/6F\delta_{ccl} + M_{H_2O}(\tilde{R}_{dv} - \tilde{R}_{vl}) \end{cases}$	CDL/CMPL CCL
Mole generation rate of species	$\dot{R}_{O_2,g} = \begin{cases} 0 \\ -\dfrac{j_c}{4F} \end{cases}, \dot{R}_{WV,g,c} = \begin{cases} -\tilde{R}_{vl} \\ \tilde{R}_{dv} - \tilde{R}_{vl} \end{cases}$	CDL/CMPL CCL
	$\dot{R}_{M,l,a} = \begin{cases} -\dot{R}_{MV,g} \\ -\dfrac{j_a}{6F} - \dot{R}_{MV,g} - \dfrac{I_p}{6F\delta_{acl}} \end{cases}, \dot{R}_{WV,g,a} = \begin{cases} -\tilde{R}_{vl} \\ \tilde{R}_{dv} - \tilde{R}_{vl} \end{cases}$	ADL/AMPL ACL
	$\dot{R}_{MV,g} = A_{lg}h_{lg}s(1-s)\dfrac{(p_{MV}^{sat} - p_{MV})}{RT}$	ADL/AMPL/ACL

fusion coefficients for each species, the interfacial transfer rates of methanol between liquid and gas phases and all the other source terms. All these correlations and associated nomenclatures are listed in Table 2.

2.4. Boundary and interfacial conditions for mass transport

As indicated in Fig. 1, the computational domain is enclosed by eight boundaries/interfaces. The conditions at each boundary/interface are described below.

Boundary I: This boundary represents the inlet of reactant supply at the anode, at which the concentration of liquid methanol, liquid-phase pressure, liquid saturation and the concentrations of methanol vapor and water vapor are all specified to be inlet conditions:

$$C_{M,l} = C_M^{in}, C_{MV} = C_{MV}^{in}, C_{WV} = C_{WV,a}^{in}, p_l = p_l^{in}, s = 1 \quad (26)$$

Interface III and VI: These two boundaries are the interfaces between MPLs and CLs for the anode and cathode, which indicate impermeable walls for the dissolved water since there exists no electrolyte in the MPLs. Accordingly, the fluxes of the dissolved water in the x direction are zero at these interfaces:

$$N_W|_+ = 0 \text{(III)}, \quad N_W|_- = 0 \text{(VI)} \quad (27)$$

Interface IV: This interface is the interface between the ACL and the membrane for the anode, which is impermeable for both the gas and the liquid (except methanol in the liquid). Thus, all the fluxes except the dissolved water and methanol in the liquid in the x direction are zero at this interface:

$$\left.\frac{\partial p_{l,a}}{\partial x}\right|_- = 0, \left.\frac{\partial p_{g,a}}{\partial x}\right|_- = 0, \left.\frac{\partial C_{WV,g,a}}{\partial x}\right|_- = 0, \left.\frac{\partial C_{MV,g}}{\partial x}\right|_- = 0 \quad (28)$$

Interface V: This interface is the interface between the CCL and the membrane for the cathode. It is assumed that the methanol transported from the anode will be depleted immediately due to the very fast methanol reaction at the cathode, and thus the methanol concentration at this interface is zero. Similar to interface IV, all the gas and liquid fluxes in the x direction are zero at this interface:

$$C_{M,l}|_- = 0, \left.\frac{\partial p_{l,c}}{\partial x}\right|_+ = 0, \left.\frac{\partial p_{g,c}}{\partial x}\right|_+ = 0, \left.\frac{\partial C_{WV,g,c}}{\partial x}\right|_+$$

$$= 0, \left.\frac{\partial C_{O_2}}{\partial x}\right|_+ = 0 \quad (29)$$

Boundary VIII: This boundary represents the inlet of oxygen supply at the cathode, at which the following boundary conditions are specified:

$$C_{O_2} = C_{O_2}^{in}, C_{WV} = C_{WV,c}^{in}, p_g = p_g^{in}, s = 0 \quad (30)$$

Table 3
Cell geometric dimensions and operating parameters

Parameters	Symbols	Value	Unit
Anode diffusion layer thickness	δ_{adl}	2.6×10^{-4}	m
Anode micro-porous layer thickness	δ_{ampl}	0.3×10^{-4}	m
Anode catalyst layer thickness	δ_{acl}	0.2×10^{-4}	m
Membrane thickness (Nafion 115)	δ_{mem}	0.5×10^{-4}	m
Cathode diffusion layer thickness	δ_{cdl}	2.6×10^{-4}	m
Cathode micro-porous layer thickness	δ_{cmpl}	0.3×10^{-4}	m
Cathode catalyst layer thickness	δ_{ccl}	0.2×10^{-4}	m
Operation temperature	T	333.15	K
Anode inlet pressure	p_l^{in}	1.013×10^5	Pa
Cathode inlet pressure	p_g^{in}	1.013×10^5	Pa
Inlet methanol concentration at anode	C_M^{in}	1000	mol m^{-3}
Inlet methanol vapor concentration at anode	C_{MV}^{in}	C_{MV}^{sat}	mol m^{-3}
Inlet oxygen concentration at cathode	$C_{O_2}^{in}$	7.68	mol m^{-3}
Inlet water vapor concentration at anode	$C_{WV,a}^{in}$	p_{vapor}^{sat}/RT	mol m^{-3}
Inlet water vapor concentration at cathode	$C_{WV,c}^{in}$	p_{vapor}^{sat}/RT	mol m^{-3}
Inlet liquid saturation at anode	s^{in}	1	–
Inlet liquid saturation at cathode	s^{in}	0	–

Besides, the conditions at the interfaces II, III, VI and VII for the gas and liquid transport in the porous region and at interfaces IV and V for the dissolved water transport in the electrolyte are given based on the principle that the continuity and mass/species flux balance are required at each interface to satisfy the general mass and species conservation of the entire cell. It should be pointed out here that since the anode gas and liquid pressure, as well as the anode capillary pressure, is continuous at interfaces II and III, so is the cathode gas and liquid pressure at interfaces VI and VII, the difference in the characteristics of DL, MPL and CL causes discontinuities in the liquid saturation at these four interfaces.

2.5. Electrochemical kinetics

On the DMFC anode, the Tafel-like expression is used to model the kinetics of methanol oxidation reaction (MOR):

$$j_a = A_{v,a} j_{0,MeOH}^{ref} \left(\frac{C_M}{C_{MeOH}^{ref}} \right)^{\gamma} \exp \left(\frac{\alpha_a F}{RT} \eta_a \right) \tag{31}$$

where the reaction order γ is related to the methanol concentration and assumed to be the zero-order when methanol concentration is higher than a reference value. Otherwise, the first-order reaction is specified.

With respect to the oxygen reduction reaction (ORR) on the cathode, the Tafel-like expression gives [13,15]:

$$j_c = (1 - s) A_{v,c} j_{0,O_2}^{ref} \left(\frac{C_{O_2}}{C_{O_2}^{ref}} \right) \exp \left(-\frac{\alpha_c F}{RT} \eta_c \right) \tag{32}$$

2.6. Current balance, cell voltage and water balance

The protons and electrons produced by the MOR on the anode transfer to the cathode through the membrane and the external circuit, respectively. The cell current density can be calculated by

$$I = \int_{ACL} j_a \, dx \tag{33}$$

To account for methanol crossover, the 'parasitic' current density is used to express the rate of methanol crossover:

$$I_p = 6F N_{M,l} \tag{34}$$

where the molar flux of methanol crossover, $N_{M,l}$, is given by Eq. (25).

On the cathode, it is assumed that both the cell current and the 'parasitic' current are entirely consumed by the ORR, i.e.:

$$I + I_p = \int_{CCL} j_c \, dx \tag{35}$$

In summary, for a given anode overpotential, η_a, the cell current density, I, and the 'parasitic' current density, I_p, can be determined from Eqs. (33) and (34), respectively. Then, the cathode mixed overpotential, η_c, with the effect of methanol crossover, can be obtained from Eqs. (32) and (35). Finally, the cell voltage can be determined from:

$$V_{Cell} = V_0 - \eta_a + \eta_c - I \left(R_{Contact} + \frac{\delta_{mem}}{\kappa} \right) \tag{36}$$

where V_0, $R_{Contact}$ and κ denote the thermodynamic equilibrium voltage of a DMFC, the contact resistance and the proton conductivity of the membrane, respectively.

Finally, the flux of water crossover with the effect of diffusion ($N_{W,diff}$), electro-osmotic drag ($N_{W,eo}$) is determined using the values at the interface IV:

$$N_{W,diff} = -\varepsilon_e^{1.5} D_{we}(\lambda) \nabla C_{we}|_+ \tag{37}$$

$$N_{W,eo} = +n_{d,H_2O} \frac{I}{F}\bigg|_+ \tag{38}$$

And the total flux of water crossover is also represented by the so-called net water-transport coefficient, α, which is given

by:

$$\alpha = \frac{N_W F}{I} \qquad (39)$$

The above-described governing equations for the cell geometric dimensions and operating parameters listed in Table 3 subjected to electrochemical properties listed in Table 1, were solved numerically using a self-written code, which was developed based on the SIMPLE algorithm with the finite-volume-method [16,17].

3. Results and discussion

3.1. Distributions and various species at different current densities

This section presents the distributions of several species, including concentration of methanol solution, cathode oxygen concentration, anode gas pressure and liquid saturation, cathode liquid pressure and liquid saturation, and the water content in the electrolyte region, at different current densities.

Fig. 3a shows the distribution of methanol concentration in the DMFC anode and the membrane at different current densities. It can be seen that at a given current density the methanol concentration decreases in each layer and reaches zero at the PEM/CCL interface. The different slopes of methanol concentration across different porous layers (ADL, AMPL, ACL, and PEM) indicate the different effective diffusivities of methanol (D_M^{eff}) in different layers. Fig. 3a also shows that with the increase in current density, methanol concentration decreases in all the layers as more methanol is consumed in the ACL. When the current density reaches about 484.0 mA cm^{-2} ($\eta_a = 0.6$ V), methanol concentration approaches almost zero in the ACL, meaning that methanol is almost completely consumed in the ACL and correspondingly, 484.0 mA cm^{-2} is just the methanol-transport-controlled limiting current density.

The distribution of gas oxygen concentration in the cathode porous region at different current densities is shown in Fig. 3b.

Oxygen is transported through the gas pores from the cathode channel to the CCL, in which the oxygen concentration becomes lower due to the consumption of oxygen by the ORR. With the increase in current density, the oxygen concentration is also reduced due to the increased oxygen consumption. However, the decrease in oxygen concentration from the channel to the CL is relatively small even at the largest current density, indicating that the mass transport resistance of oxygen is rather low. This is due to faster transport of oxygen in the gas phase and lower liquid water saturation in the cathode porous region, as will be discussed later.

The distribution of gas pressure in the anode at different current densities is shown in Fig. 4a. Due to the hydrophobic characteristic of the anode porous region, the gas pressure is smaller than the anode liquid pressure, which is nearly a constant of 101.3 kPa. It can be seen that the gas pressure can vary greatly from the anode channel to the ACL. Apparently, the gas pressure in the region close to the PEM is higher than that in the region close to the anode flow channel, as gas CO_2, generated by MOR in the ACL, is transferred from the ACL to the flow channel. Across the interfaces II and III the gas pressure is continuous while the gradients are different due to the different properties (K and k_{rg}) at different layers, which can be understood by referring to Eq. (12). With the increase in current density, the gas pressure increases due to the increased generation of gas CO_2. It should be pointed out here that in the ACL the gas pressure does not always decrease from the interface IV to III, and this anomalous distribution is caused by the complicated mass exchanges between different phases (i.e., gas, liquid, dissolved phase) in the CL. By referring to Eq. (12) and the corresponding source terms for the gas transport, there exists not only the CO_2 generation and water vapor gaining from the desorption of dissolved water into the gas phase, but also the water vapor loss by condensing into the liquid phase in the CL. The fluxes of water exchange depend highly on the local water status (e.g., concentrations of water vapor and dissolved water), which in turn affects the anomalous distribution of gas pressure.
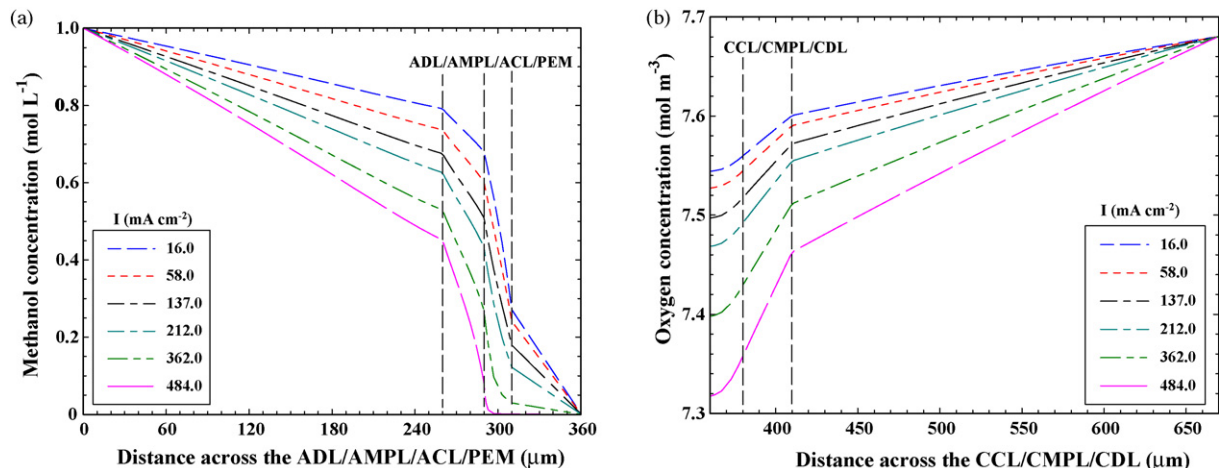

Fig. 3. Distributions of (a) methanol concentration in liquid phase through the anode electrode and membrane, and (b) gas oxygen concentration through the cathode at different current densities.
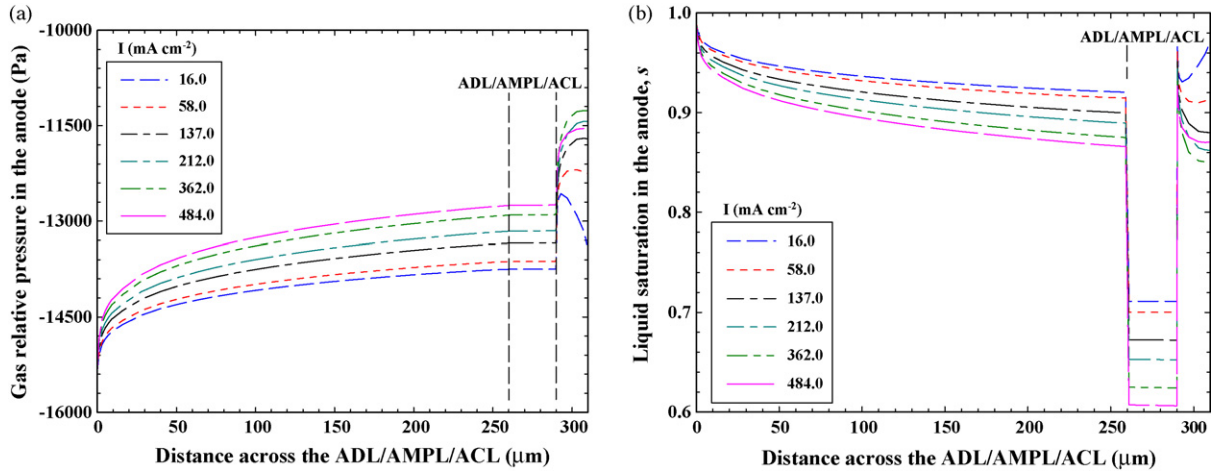
Fig. 4. Distributions of (a) gas pressure in the anode, and (b) liquid saturation in the anode at different current densities.

The corresponding distribution of anode liquid saturation at different current densities is shown in Fig. 4b. It is seen that anode liquid saturation is always smaller than 1.0 in the porous region due to the generation of CO_2. It deceases from the channel across the ADL as the liquid is transported from the channel to the CL. It is clear that there is a discontinuity of anode liquid saturation at the interface II, which is caused by the continuity of capillary pressure across the interface. At the interface II, from the definition of capillary pressure (Eq. (20)), it gives:

$$\cos \theta_{ADL} \left(\frac{\varepsilon_{ADL}}{K_{ADL}} \right)^{0.5} J(s_{ADL,II})$$
$$= \cos \theta_{AMPL} \left(\frac{\varepsilon_{AMPL}}{K_{AMPL}} \right)^{0.5} J(s_{AMPL,II}) \qquad (40)$$

Thus, the large differences in permeability and porosity between the ADL and AMPL cause a discontinuity in the liquid saturation across the interface of these two layers. Since the permeability of the MPL is extremely small, the liquid saturation in this finer porous region is rather low (~0.6–0.7). Similarly, due to the large difference in permeability and contact angle

between the AMPL and ACL, a discontinuity in the liquid saturation occurs across the interface III, and the less hydrophobic property (θ) of the ACL mainly contributes to the relatively high liquid saturation (~0.85–0.95). With the increase in current density, the anode liquid saturation is reduced due to the increased generation of gas CO_2. Generally, the gas phase in the anode porous region has two effects: on one hand, it limits the access of methanol from the channel to the catalyst region; on the other hand, the gas occupancy in the catalyst layer reduces the water content in the electrolyte and thus influences the water crossover from the anode to the cathode, as will be discussed later.

The gas pressure in the cathode is also nearly a constant of 101.3 kPa, while the liquid pressure can vary greatly from the cathode channel to the CCL, which is shown in Fig. 5a. Due to the hydrophobic characteristic of the cathode porous region, the liquid pressure is larger than the cathode gas pressure. It is seen that the liquid pressure increases from the cathode channel to the CCL due to the fact that liquid water is transported out from the CCL to the cathode channel. Similar to the anode gas pressure, the cathode liquid pressure is continuous across the interfaces VI and VII while the gradients are different due to the different diffusivities (K and k_{rl}) at different layers, which
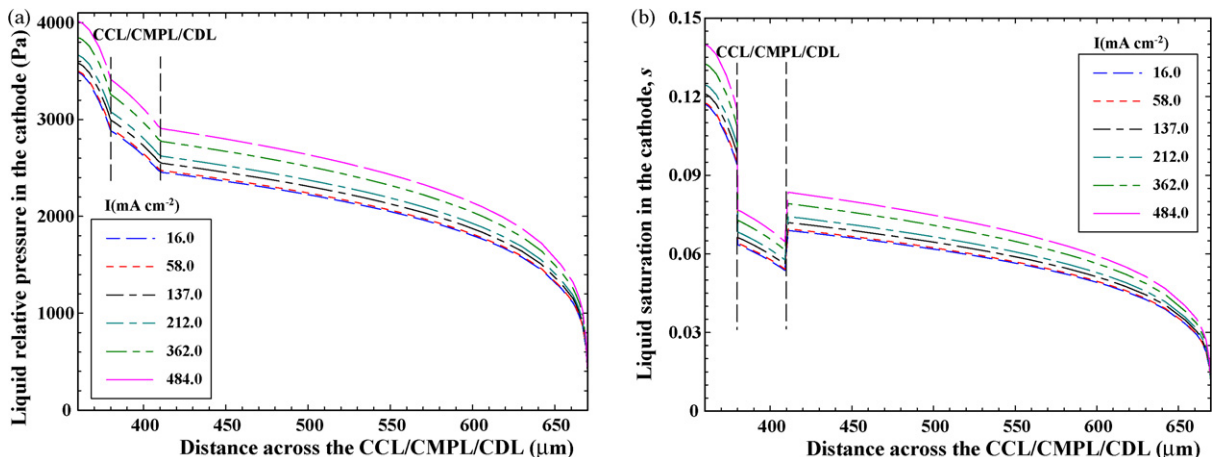

Fig. 5. Distributions of (a) liquid pressure in the cathode, and (b) liquid saturation in the cathode at different current densities.

can be understood by referring to Eq. (17). With the increase in current density, the liquid pressure also increases due to the increased water generation from the ORR and water crossover in the CCL. Since the liquid pressure in the anode is nearly a constant (101.3 kPa), the liquid pressure in the cathode is always larger, and the induced back convection of water from the cathode to the anode is utilized to reduce the water crossover in the DMFC.

The corresponding distribution of cathode liquid saturation at different current densities is shown in Fig. 5b. It is seen that cathode liquid saturation is rather small (<0.15) in the cathode porous region, accordingly the mass transport resistance of oxygen is rather small (see Fig. 3b). The liquid saturation increases from the cathode channel across the CDL, and similar to the anode liquid saturation, it shows a discontinuity at the interface VII, which is caused by the large difference in permeability and porosity between the CMPL and the CDL. The much smaller permeability of the CMPL mainly results in the lower liquid saturation in this finer porous region. Similarly, a discontinuity in the liquid saturation occurs at the interface VI, and the less hydrophobic property (θ) of the CCL leads to the relatively high liquid saturation. It is also found that the cathode liquid saturation increases with the increase in current density due to the increased water flux across the porous region.

Comparing Figs. 4b and 5b, it can be seen that liquid–gas two-phase flow takes place in both the ACL and the CCL, and thus the electrolyte polymer is not exactly in equilibrium with liquid water in the anode or saturated water vapor in the cathode. Accordingly, it is easy to conceive that water content across the electrolyte region is not uniform, and it depends highly on the liquid saturation in the ACL and the CCL, which in turn influences the water crossover through the membrane.

The water content, representing the dissolved water concentration from Eq. (4), across the electrolyte region (ACL, PEM and CCL) at different current densities is shown in Fig. 6a. Apparently, the distribution of water content across the electrolyte region is highly not uniform: the water content near the anode is higher than that near the cathode. For instance, at the current density of $16.0 \, \text{mA cm}^{-2}$, water content of electrolyte in

the ACL is near to 21, whereas in the CCL it is only between 13 and 15. This significant difference in water content between the ACL and the CCL is mainly due to the fact that liquid saturation in the ACL is relatively high (about 0.9 from Fig. 4b), whereas in the CCL it is rather low (about 0.12 from Fig. 5b). With the increase in current density, it is seen that water content decreases somewhat in the ACL while increases slightly in the CCL, leading to reduced gradients across the membrane as well. This change in water content is also mainly caused by the slight change in liquid saturation with current density: liquid saturation decreases in the ACL (Fig. 4b) while increases in the CCL (Fig. 5b) with the increase in current density. The non-uniform distribution of water content and its variation with current density shown in Fig. 6a clearly demonstrate that water content across the electrolyte region highly depends on the liquid saturation in both the ACL and the CCL. It is also noted that near the limiting current density ($484 \, \text{mA cm}^{-2}$) water content across the ACL increases first from the AMPL/ACL interface (III) and then decreases, which is different from the continuous decrease at relatively low current densities. This anomalous behavior is due to that near the limiting current density, the generated current across the ACL is highly not uniform: current is mainly generated near the interface III. The generated current in the region near the interface III can lead to a considerable analogous dissolved water "loss" by the effect of electro-osmotic drag, which can be understood by referring to Eq. (23).

Based on the water content distribution shown in Fig. 6a, we can now examine how the flux of water crossover varies with current density by studying Fig. 6b. It is seen that the total flux of water crossover increases first slowly and then faster with the increase in current density, which is consistent with the experimental data reported elsewhere [1,2]. As discussed in the preceding section, the total flux is due to three water-crossover mechanisms: diffusion flux, electro-osmotic drag flux and back-flow flux. First, it is seen that the water flux by electro-osmotic drag increases nearly linearly with current density. Secondly, the diffusion flux from the anode to the cathode is quite substantial, which is due to that the water content at the anode is much higher than that at the cathode (Fig. 6a). With the increase
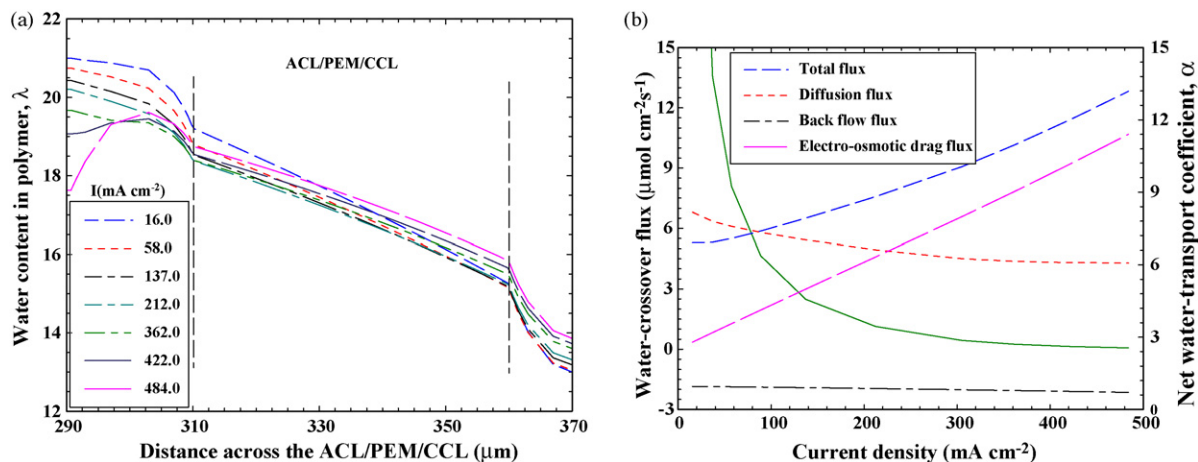

Fig. 6. Distribution of water content in the electrolyte region at different current densities (a), and variation in the water-crossover flux through the membrane and the corresponding net water-transport coefficient with current density (b).

in current density, the diffusion flux decreases as a result of the decreased water content in the anode and the increased water content in the cathode, as shown in Fig. 6a. Hence, the assumption of uniform water content across the membrane made in many previous papers on modeling DMFCs will cause significant errors in predicting water crossover and cell performance. Third, the back-flow flux from the cathode to the anode, indicating by the negative value, is slightly enhanced with current density, which is due to the increased liquid pressure difference across the membrane as shown in Fig. 5a. Fig. 6b also shows the corresponding net water-transport coefficient, α, which is determined from Eq. (39). It is seen that α decreases rapidly at low current densities, but the decrease becomes slower at high current densities, from about 15 to 2.6 when the current density is increased from 35.0 to 400.0 mA cm^{-2}. It is worth mentioning here that the variation trends of the water-crossover flux by different transport mechanisms, as well as the corresponding α, are all consistent with the experimental results in our previous work [1,2].

3.2. Effect of contact angle of the cathode MPL

From the results shown in Figs. 4–6, it is clear that the properties of cathode porous region have great effects on water crossover through the membrane, due to the fact that the flux of water crossover depends both on the liquid pressure built up in the cathode and on the liquid saturation in the CCL. From Eqs. (17) and (20), we can obtain:

$$u = -\frac{Kk_{rl}}{\mu_l/\rho_l}\nabla p_{l,c} = \frac{\sigma \cos\theta(\varepsilon K)^{0.5}k_{rl}}{\mu_l/\rho_l}\frac{dJ(s)}{ds}\nabla s \quad (41)$$

which shows that the liquid pressure and liquid saturation in the cathode can be significantly affected by the permeability, contact angle, porosity and thickness of the cathode porous layer, especially the CMPL. In this section, the effect of contact angle of CMPL is discussed.

The contact angle of the CMPL varies from 110° to 150°, indicating relatively low to high hydrophobic level, while all the

Table 4
Limiting current densities under different parameters ($\eta_a = 0.6$ V)

Limiting current density (mA cm^{-2})		
	110°	484.6
	120°	484.2
Effect of contact angle of CMPL	130°	483.5
	140°	482.6
	150°	481.9
	15 μm	484.5
Effect of thickness of CMPL	30 μm	484.2
	60 μm	483.6
	90 μm	483.1
	5.0e–13 m^2	484.7
	2.5–13 m^2	484.2
	1.0e–13 m^2	480.3
Effect of permeability of CMPL	0.75e–13 m^2	477.4
	0.5e–13 m^2	470.1
	0.4e–13 m^2	462.8
	0.3e–13 m^2	449.7
	0.25e–13 m^2	438.9
	93°	454.2
	94°	471.7
	95°	477.4
	97°	481.4
Effect of contact angle of CCL	100°	483.2
	105°	483.6
	110°	483.1
	120°	481.8

other parameters are kept the same as listed in Tables 1 and 3. Fig. 7a shows the distribution of cathode liquid pressure with different CMPL contact angles at nearly the same limiting current densities (~484.0 mA cm^{-2} as shown in Table 4). Apparently, the increase in the liquid pressure across the CMPL becomes more rapidly with the increase in the contact angle, which also leads to increased liquid pressure built up in the CCL. This indicates that using highly hydrophobic CMPL helps build up a higher liquid pressure in the CCL and thus enhance the water back flow from the cathode to the anode. From Eq. (41), the higher liquid pressure gradient in the CMPL with a larger contact angle comes from the reduced liquid saturation, as shown
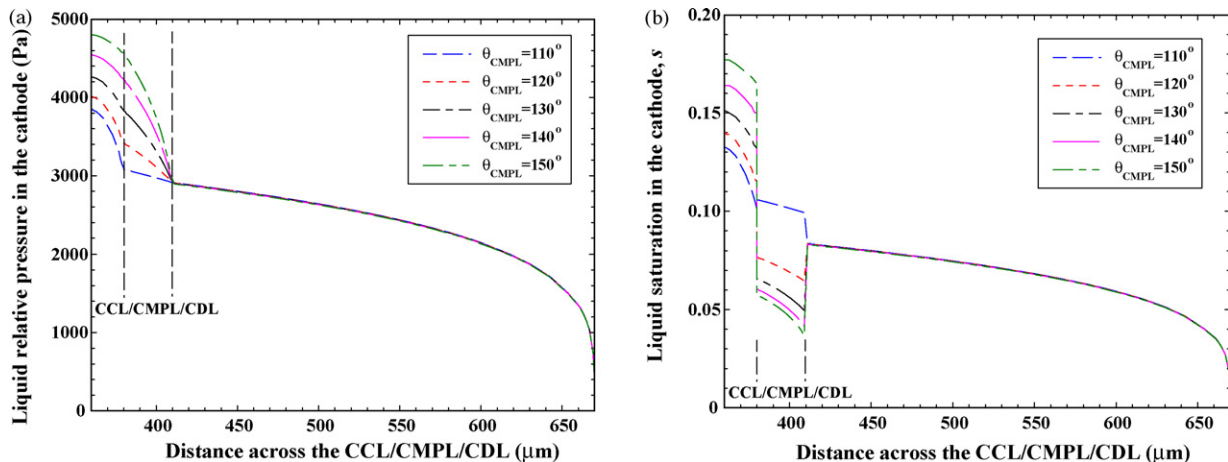

Fig. 7. Distributions of (a) liquid pressure in the cathode, and (b) liquid saturation in the cathode with different contact angles of the CMPL and at the limiting current densities ($\eta_a = 0.6$ V).
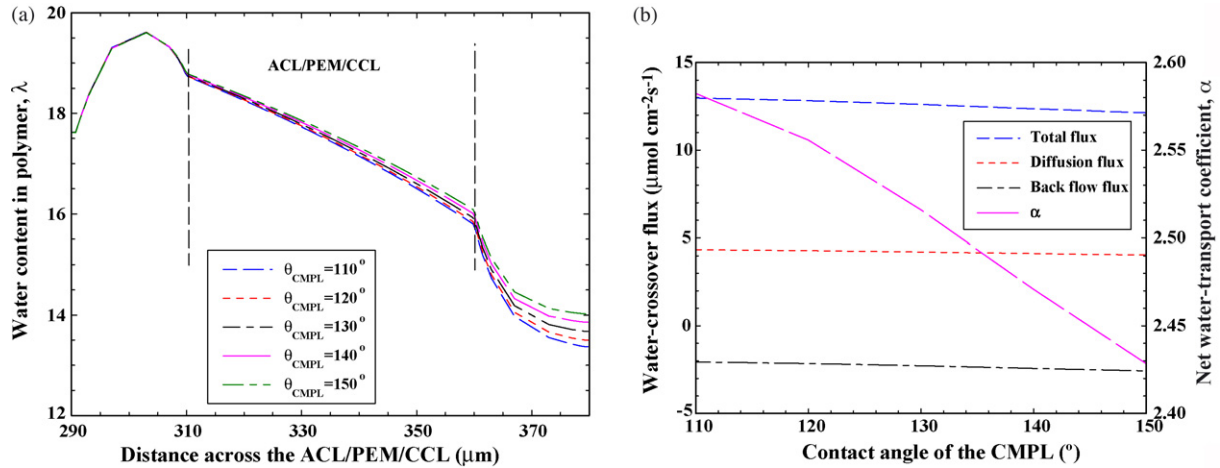
Fig. 8. Distribution of water content in the electrolyte region with different contact angles of the CMPL and at the limiting current densities ($\eta_a = 0.6$ V) (a), and the corresponding variation in the water-crossover flux through the membrane and the net water-transport coefficient (b).

in Fig. 7b. It is seen that the liquid saturation in the CMPL is reduced from about 0.10 to 0.05 when the contact angle is increased from 110° to 150°, due to the enhanced hydrophobic level. However, the liquid saturation in the CCL is increased from about 0.12 to 0.17, which is caused by the increased liquid pressure in the CCL. This result indicates that increasing the hydrophobic level of the CMPL helps to reduce the water saturation across it, which is beneficial for the oxygen transport through it, while the accordingly increased liquid pressure built up in the CCL enhances the water flooding in the CL.

The water content across the electrolyte region with different contact angles of the CMPL is shown in Fig. 8a. With the contact angle increasing from 110° to 150°, water content in the CCL increases somewhat, which is due to the increased liquid saturation in the CCL, as shown in Fig. 7b. As a result, the gradient of water content across the membrane is slightly reduced. Accordingly, the change in the cathode liquid pressure and the water content in the polymer caused by the change in the CMPL contact angle will affect the flux of water crossover from the anode to the cathode, which is shown in Fig. 8b. It can be seen

that with the increase in the CMPL contact angle, the water flux by diffusion from the anode to the cathode is slightly reduced due to the lowered gradient of water content across the membrane, while the water flux by back flow from the cathode to the anode is slightly increased due to the enhanced liquid water pressure difference between the cathode and the anode. As a result, the total flux of water crossover from the anode to the cathode as well as the corresponding net water-transport coefficient is slightly reduced. However, it is clear that the reduction of water crossover caused by the increased CMPL contact angle is rather small, possibly indicating that the water crossover from the anode to the cathode is not very sensitive to the contact angle of the hydrophobic CMPL.

3.3. Effect of thickness of the cathode MPL

The effect of thickness of the CMPL is studied by changing the thickness from 15 to 90 μm, while keeping all the other parameters the same, as listed in Tables 1 and 3. Fig. 9a shows the distribution of cathode liquid pressure with different
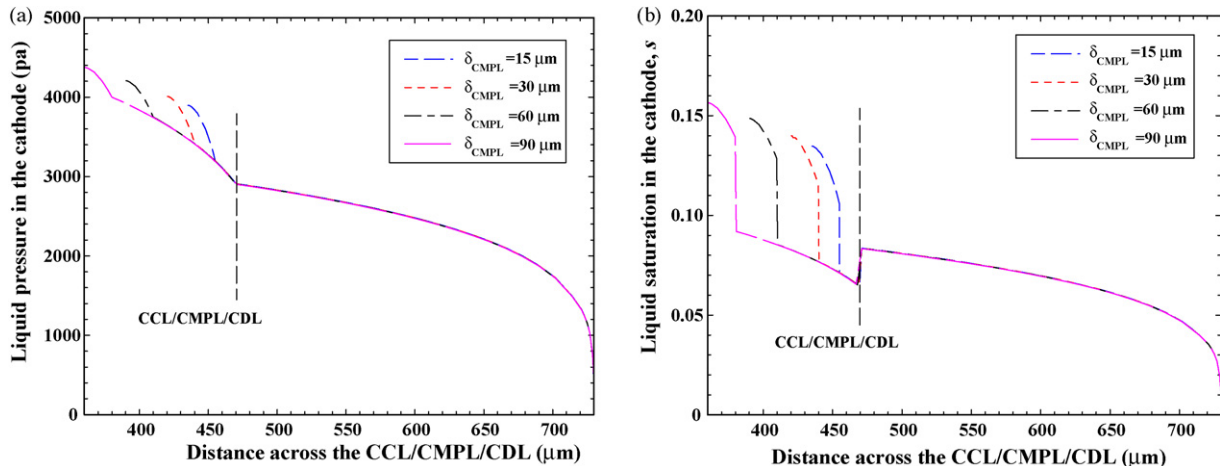

Fig. 9. Distributions of (a) liquid pressure in the cathode, and (b) liquid saturation in the cathode with different thicknesses of the CMPL and at the limiting current densities ($\eta_a = 0.6$ V).
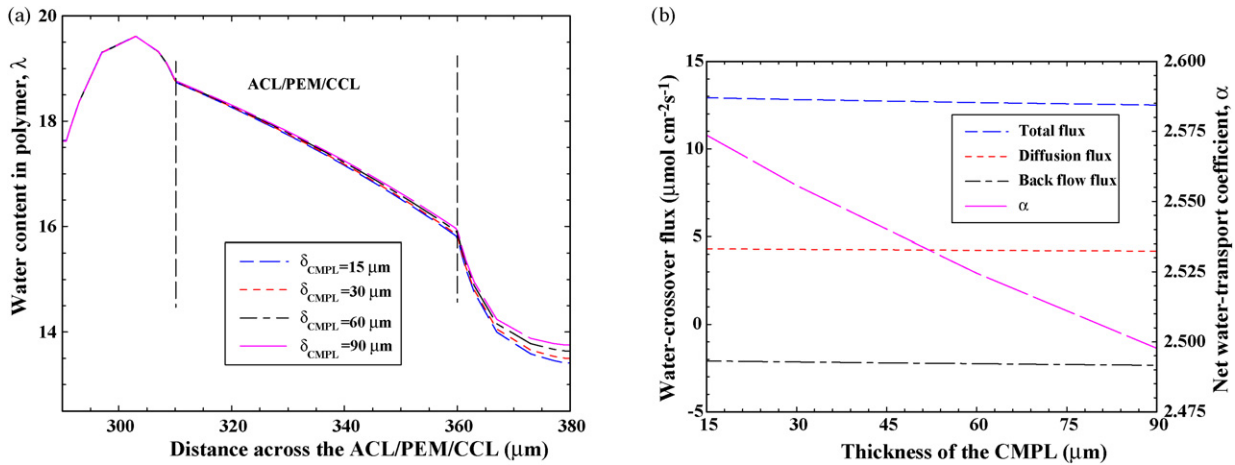
Fig. 10. Distribution of water content in the electrolyte region with different thicknesses of the CMPL and at the limiting current densities ($\eta_a = 0.6$ V) (a), and the corresponding variation in the water-crossover flux through the membrane and the net water-transport coefficient (b).

CMPL thicknesses at nearly the same limiting current densities ($\sim$484.0 mA cm^{-2} as shown in Table 4). It is seen that the gradients of the increase in the liquid pressure across the CMPL for different CMPL thicknesses are nearly the same due to the same properties, but a thicker CMPL can build up a higher liquid pressure due to the longer transport route, which also leads to an increased liquid pressure built up in the CCL. This indicates that increasing thickness of the CMPL is beneficial for building up a higher liquid pressure in the CCL and thus enhancing the water back flow from the cathode to the anode. The corresponding liquid saturation in the cathode is shown in Fig. 9b. Similarly, the gradients of the increase in the liquid saturation across the CMPL for different CMPL thicknesses are also the same, but thicker CMPLs can lead to larger liquid saturation near the CCL/CMPL interface (VI). For instance, at the interface VI, liquid saturation in the CMPL for the thickness of 15 μm is about 0.07, which is smaller than that in the CDL near the interface VII, while for the thickness of 90 μm it is about 0.09, which is larger than that in the CDL near the interface VII. It is also found that the liquid saturation in the CCL increases with the CMPL thickness, due to the increased liquid pressure in the CCL. The increased liquid pressure shown in Fig. 9a and the increased liquid saturation in the CCL shown in Fig. 9b will obviously affect the water crossover through the membrane.

The water content across the electrolyte region with different CMPL thicknesses is shown in Fig. 10a. Water content in the CCL is increased slightly due to the increased liquid saturation in the CCL, as shown in Fig. 9b, which leads to a slight decrease in the gradient of water content across the membrane. The change in the water-crossover flux with the increase in the CMPL thickness is shown in Fig. 10b. It is also found that the water-crossover flux by diffusion is slightly reduced with the increase in the thickness due to the lowered water content gradient across the membrane, but the water-crossover flux by back flow is slightly increased due to the enhanced liquid water pressure difference between the anode and the cathode. Accordingly, the total flux of water crossover as well as the corresponding net water-transport coefficient is slightly reduced. The rather

small change in the water-crossover flux with the increase in the CMPL thickness possibly indicates that the water crossover through the membrane is also not very sensitive to the thickness of the hydrophobic CMPL. At the same time, it should be noted that increasing the CMPL thickness will lead to a larger oxygen transport resistance in both the CMPL and the CCL, due to the increased liquid saturation, as shown in Fig. 9b.

3.4. Effect of permeability of the cathode MPL

The effect of permeability of the CMPL is examined by changing its value from 5.0×10^{-13} to 0.25×10^{-13} m^2, while keeping all the other parameters the same, as listed in Tables 1 and 3. Fig. 11a shows the distribution of cathode liquid pressure with different permeabilities of the CMPL at the limiting current densities (shown in Table 4). It is seen that the increase in the liquid pressure across the CMPL can become much more rapidly with the decrease in the CMPL permeability. For instance, the liquid pressure increases slightly from 2.9 to 3.0 kPa across the CMPL for the permeability of 5.0×10^{-13} m^2, whereas it can increase about four times from about 2.6 to 10.8 kPa across the CMPL for the permeability of 0.25×10^{-13} m^2. As a result, the liquid pressure in the CCL is significantly enhanced with the reduction of the CMPL permeability.

The corresponding liquid saturation in the cathode is shown in Fig. 11b. It is seen that with the permeability decreasing from 5.0×10^{-13} to 1.0×10^{-13} m^2, the liquid saturation in the CMPL is evidently decreased. However, when the permeability is reduced below 1.0×10^{-13} m^2, the change in the saturation in the CMPL is rather small. In the CCL, the liquid saturation is increased significantly from about 0.12 to 0.84 with the decrease in the CMPL permeability. This sharp increase in the liquid saturation is due to the significantly enhanced liquid pressure in the CCL, and it obviously increases the risk of water flooding. The sharply increased liquid saturation in the CCL can lead to two effects. On one hand, it increases the oxygen transport resistance through the CCL due to the reduced gas void
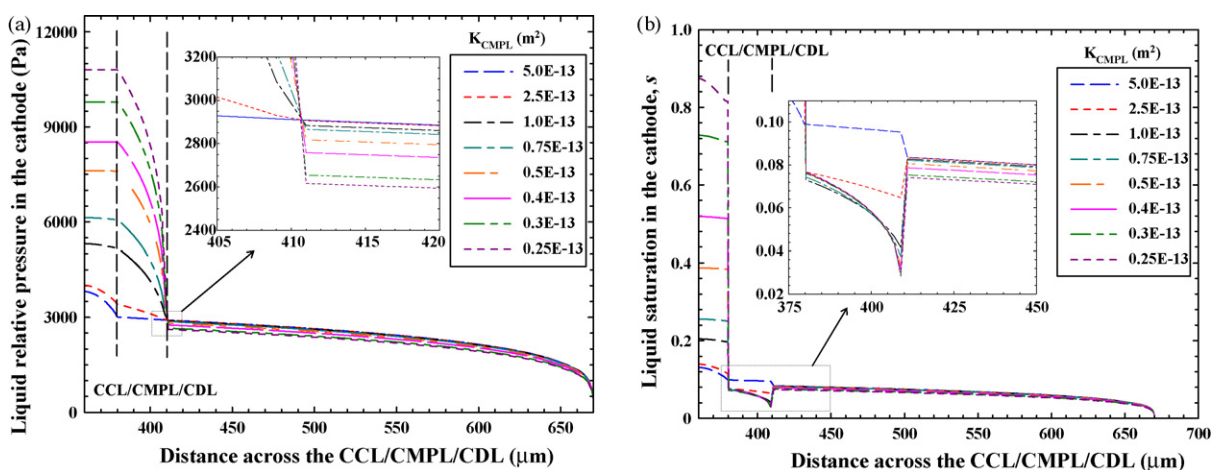
Fig. 11. Distributions of (a) liquid pressure in the cathode, and (b) liquid saturation in the cathode with different permeabilities of the CMPL and at the limiting current densities ($\eta_a = 0.6$ V).

fraction, which can be proved by the reduced oxygen concentration in the CCL, as shown in Fig. 12. On the other hand, the effective catalyst sites available for ORR reaction are seriously reduced due to the increased coverage by liquid water. These two effects result in increased mass transport polarization and thus reduced cell performance. From Table 4, it can be seen that the limiting current density can be decreased from about 484.0 to 439.0 mA cm^{-2} due to the increased liquid saturation in the CCL.

The water content across the electrolyte region with different CMPL permeabilities is shown in Fig. 13a. Due to the highly increased liquid saturation in the CCL, it is seen that water content in the CCL is also highly increased from about 13.5 for the permeability of 5.0×10^{-13} m^2 to about 21 for the permeability of 0.25×10^{-13} m^2, which is even higher than that in the anode side. Accordingly, the gradient of water content across the membrane is also reduced greatly. The change in the water-crossover flux with the effect of the CMPL permeability is shown in Fig. 13b. It can be seen that the total water-crossover

flux as well as the flux by diffusion only decreases slightly when the CMPL permeability is reduced from 5.0×10^{-13} to 1.0×10^{-13} m^2. However, when the permeability is reduced below 1.0×10^{-13} m^2, the water flux by diffusion is decreased sharply, and it can even become negative, indicating diffusing from the cathode to the anode. This rapidly change in the diffusion flux is caused by the significantly increased water content in the CCL. On the other hand, the highly enhanced liquid pressure in the CCL leads to a rapid increase in the flux of back flow from the cathode to the anode. As a result, when the permeability is reduced from 1.0×10^{-13} to 0.25×10^{-13} m^2, the total water-crossover flux can decrease greatly from about 11.5 to 3.3 μmol cm^{-2} s^{-1}, and the corresponding net water-transport coefficient is reduced significantly from about 2.4 to 0.8.

Apparently, decreasing the permeability of the CMPL is a very effective way to build up high liquid pressure in the CCL and thus reduce the water crossover from the anode to the cathode. However, the induced relatively high liquid saturation in the CCL is not beneficial for the oxygen transport and cell performance. In fact, the liquid saturation in the CCL can be adjusted by changing the hydrophobic level or the contact angle of the CCL, as discussed in the next section.

3.5. Effect of contact angle of the cathode CL

This section presents the effect of contact angle of the CCL on water crossover. The contact angle is changed from 93° to 120°, while the permeability of the CMPL is fixed at 0.75×10^{-13} m^2 and all the other parameters are kept the same as listed in Tables 1 and 3. Fig. 14a shows the distribution of cathode liquid pressure with different contact angles of the CCL at the limiting current densities (shown in Table 4). It is seen that the increase in the liquid pressure across the CCL becomes more rapidly with the increase in the contact angle of the CCL. For instance, the liquid pressure increases negligibly from 5.70 to 5.71 kPa across the CCL for the contact angle of 93°, but it can increase over 2 times from about 6.0 to 13.5 kPa across the CCL for the
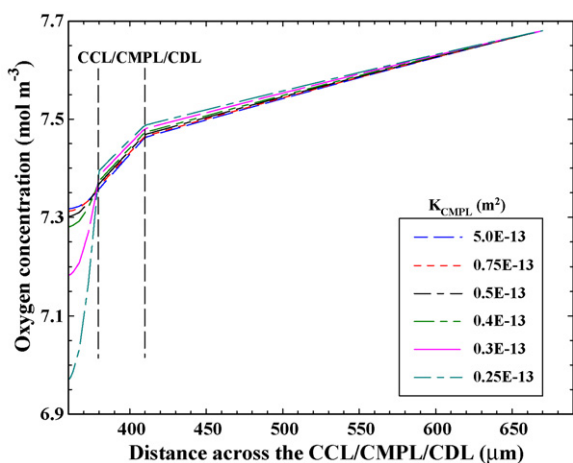

Fig. 12. Distributions of gas oxygen concentration through the cathode with different permeabilities of the CMPL and at the limiting current densities ($\eta_a = 0.6$ V).
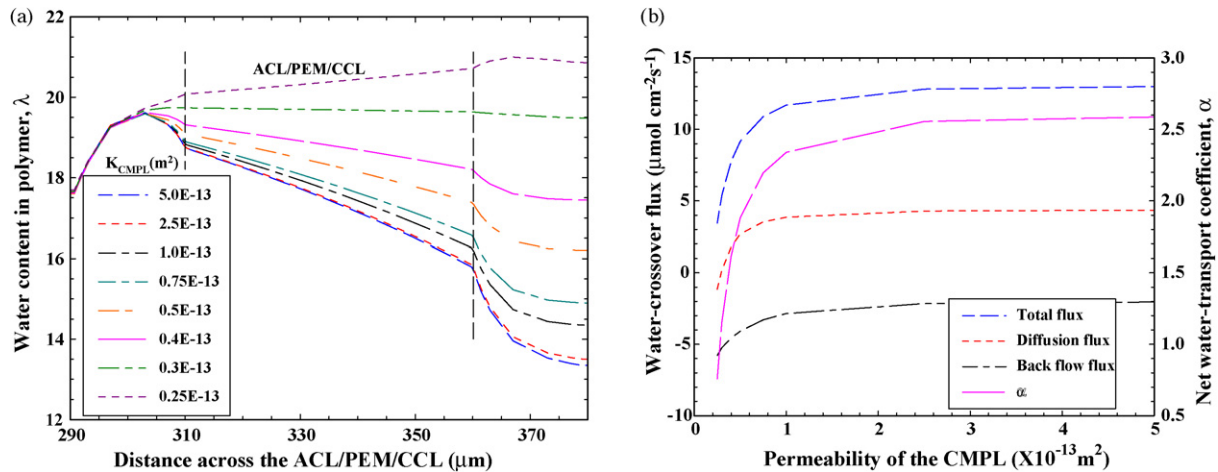
Fig. 13. Distribution of water content in the electrolyte region with different permeabilities of the CMPL and at the limiting current densities ($\eta_a = 0.6$ V) (a), and the corresponding variation in the water-crossover flux through the membrane and the net water-transport coefficient (b).

contact angle of 120°. This indicates that the liquid pressure in the CCL can also be significantly enhanced by increasing the hydrophobic level of the CCL.

The corresponding liquid saturation in the cathode is shown in Fig. 14b. With the increase in the contact angle from 93° to 110°, the liquid saturation in the CCL is significantly decreased, but the decrease in the liquid saturation becomes rather slow when the contact angle is above 110°. As such, increasing the hydrophobic level of the CCL can not only effectively build up high liquid pressure, which is beneficial for reducing water crossover, but also helps reduce the water flooding in the CCL. It can be seen from Table 4 that the limiting current density can be increased from about 454.0 to 482.0 mA cm^{-2} resulting from the reduced liquid saturation.

The water content across the electrolyte region with different contact angles of the CCL is shown in Fig. 15a. Due to the highly decreased liquid saturation in the CCL, water content in the CCL is also significantly decreased from about 19.3 for the

contact angle of 93° to about 13.5 for the contact angle of 120°. Accordingly, the gradient of water content across the membrane is also increased greatly. The increased liquid pressure and the decreased liquid saturation with the contact angle in the CCL result in an inconsistent effect on the flux of water crossover, which is shown in Fig. 15b. It is interesting to see that increasing the contact angle of the CCL can simultaneously enhance the back-flow flux from the cathode to the anode, which is beneficial for reducing water crossover, but increase the diffusion flux from the anode to the cathode, which tends to increase water crossover. This inconsistent effect leads to the result that an intermediate contact angle of about 97° yields the largest total flux of water crossover, and decreasing or increasing the contact angle can all effectively reducing the total flux of water crossover. However, from the point view of oxygen transport and cell performance, increasing the contact angle of the CCL is preferred for both lowered water crossover through the membrane and improved cell performance.
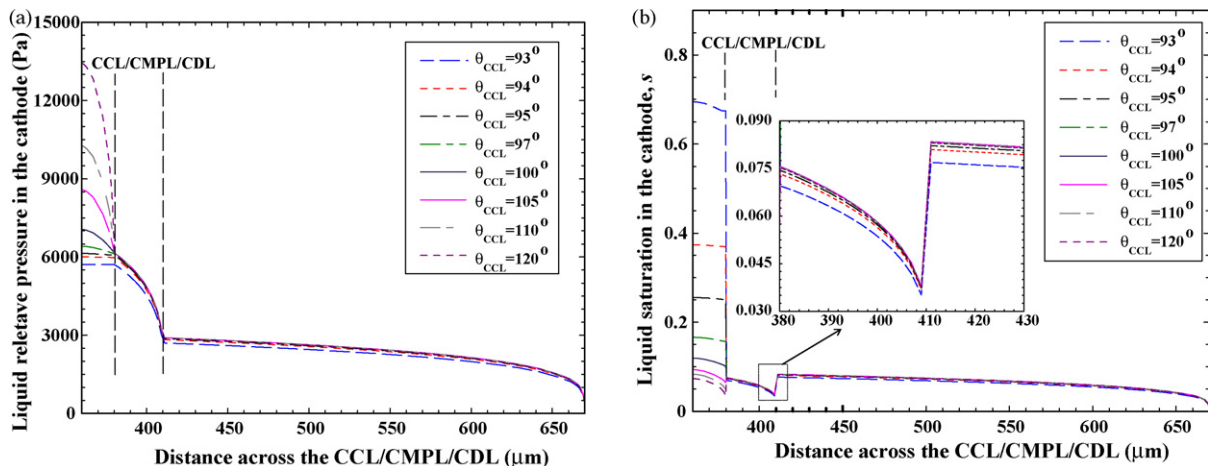

Fig. 14. Distributions of (a) liquid pressure in the cathode, and (b) liquid saturation in the cathode with different contact angles of the CCL and at the limiting current densities ($\eta_a = 0.6$ V).
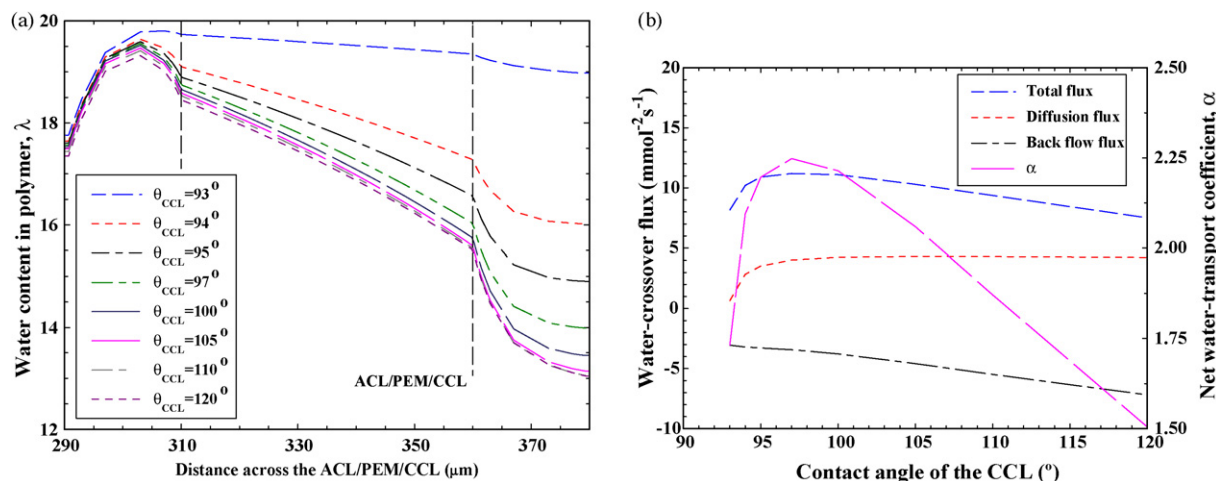
Fig. 15. Distribution of water content in the electrolyte region with different contact angles of the CCL and at the limiting current densities ($\eta_a = 0.6$ V) (a), and the corresponding variation in the water-crossover flux through the membrane and the net water-transport coefficient (b).

4. Conclusions

In this work, we present a one-dimensional, isothermal two-phase mass transport model to investigate the water transport through the membrane electrode assembly for liquid-feed DMFCs. Liquid–gas two-phase mass transport in the porous anode and cathode is modeled with classical multiphase flow theory in porous media, in which the liquid phase consists of methanol–water solution, while the gas phase includes carbon dioxide gas, methanol vapor, and water vapor. In the electrolyte region that includes the membrane and the catalyst layers (CLs), transport of dissolved water is driven by diffusion, electro-osmotic drag and convection. In particular, water transport in three phases (i.e., liquid, vapor and dissolved phase) in the CLs is coupled intrinsically, and finite-rate interfacial exchanges between different phases are introduced without any phase equilibrium assumptions. With this new model, we investigated each water-crossover mechanism through the membrane for the DMFC, and studied the effect of cathode structure, such as the design of the cathode MPL, on the water crossover through the membrane and the water ejection through the cathode. The salient findings in this work are summarized as follows:

(1) At low current densities, liquid saturation in the anode CL is in general larger than that in the cathode, resulting in a large difference in water content across the membrane and thus water diffusion from the anode to the cathode. However, on the other hand, liquid pressure in the cathode is larger than that in the anode, leading to back convection of liquid water directly from the cathode to the anode. Lowering water diffusion and enhancing water back convection through the membrane should be utilized to reduce the water crossover in the DMFC.

(2) With the increase in current density, liquid saturation decreases in the anode CL, but increases in the cathode CL. At the same time, an increase in current density also leads to an increase in liquid pressure in the cathode CL. Accordingly, the water-crossover flux by diffusion decreases significantly, although the flux by back convection increases to some extent. As a result, the net water-transport coefficient decreases rapidly at low current densities, but the decrease becomes slower at high current densities.

(3) It is found that increasing the liquid pressure in the cathode CL by lowering the permeability or increasing the contact angle or the thickness of the cathode MPL is accompanied with an increase in the liquid saturation in it, which helps reduce the water diffusion from the anode to the cathode. As a result, water crossover can be reduced significantly by lowering the permeability of the cathode MPL due to the enhanced back convection and decreased water diffusion, while the reduction of water crossover by increasing the hydrophobic level or the thickness of the cathode MPL is relatively small. Morever, lowering the permeability or increasing the hydrophobic level of the cathode MPL can reduce the water saturation in it, which is beneficial for the oxygen transport. However, it should be noted that the induced relatively high liquid saturation in the cathode CL increases the risk of electrode flooding. The liquid saturation in the cathode CL can be lowered by increasing its hydrophobic level, which is also very effective to build up high liquid pressure and thus reduce the flux of water crossover.

Acknowledgement

References

[1] C. Xu, T.S. Zhao, Y.L. He, J. Power Sources 171 (2007) 268.
[2] C. Xu, T.S. Zhao, J. Power Sources 168 (2007) 143.
[3] F.Q. Liu, G.Q. Lu, C.Y. Wang, J. Electrochem. Soc. 153 (2006) A543.
[4] C. Xu, T.S. Zhao, Electrochem. Commun. 9 (2007) 493.
[5] A. Blum, T. Duvdevani, M. Philosoph, N. Rudoy, E. Peled, J. Power Sources 117 (2003) 22.

[6] X. Ren, W. Henderson, S. Gottesfeld, J. Electrochem. Soc. 144 (1997) L267.
[7] T. Mennola, M. Noponen, T. Kallio, M. Mikkola, T. Hottinen, J. Appl. Electrochem. 34 (2004) 31.
[8] S. Ge, B. Yi, P. Ming, J. Electrochem. Soc. 153 (2006) A1443.
[9] B.S. Pivovar, Polymer 47 (2006) 4194.
[10] J. St-Pierre, J. Electrochem. Soc. 154 (2007) B88.
[11] G. Lin, T.V. Nguyen, J. Electrochem. Soc. 152 (2005) A1942.
[12] G. Murgia, L. Pisani, A.K. Shula, K. Scott, J. Electrochem. Soc. 150 (2003) A1231.
[13] Z.H. Wang, C.Y. Wang, J. Electrochem. Soc. 150 (2003) A508.
[14] J. Rice, A. Faghri, Int. J. Heat Mass Transfer 49 (2006) 4804.
[15] W.P. Liu, C.Y. Wang, J. Electrochem. Soc. 154 (2007) B352.
[16] W.W. Yang, T.S. Zhao, Electrochimica Acta 52 (2007) 6125.
[17] W.W. Yang, T.S. Zhao, J. Power Sources 174 (2007) 136.
[18] H. Yang, T.S. Zhao, Q. Ye, J. Power Sources 139 (2005) 79.
[19] C. Xu, Y.L. He, T.S. Zhao, R. Chen, Q. Ye, J. Electrochem. Soc. 153 (2006) A1358.
[20] T.E. Springer, T.A. Zawodzinski, S. Gottesfeld, J. Electrochem. Soc. 138 (1991) 2334.
[21] H. Meng, C.Y. Wang, J. Electrochem. Soc. 151 (2004) A358.
[22] G. Lin, W. He, T.V. Nguyen, J. Electrochem. Soc. 151 (2004) A1999.
[23] H. Meng, C.Y. Wang, Chem. Eng. Sci. 59 (2004) 3331.
[24] G. Lin, T.V. Nguyen, J. Electrochem. Soc. 153 (2006) A372.
[25] H. Meng, J. Power Sources 162 (2006) 426.
[26] S. Um, C.Y. Wang, J. Power Sources 156 (2006) 211.
[27] H. Meng, J. Power Sources 168 (2007) 218.
[28] H. Wu, P. Berg, X.G. Li, J. Power Sources 165 (2007) 232.
[29] A.Y. Karnik, A.G. Stefanopoulou, J. Sun, J. Power Sources 164 (2007) 590.
[30] A.A. Kulikovsky, J. Electrochem. Soc. 150 (2003) A1432.
[31] A. Vorobev, O. Zikanov, T. Shamim, J. Power Sources 166 (2007) 92.
[32] N.P. Siegel, M.W. Ellis, D.J. Nelson, M.R.V. Spakovsky, J. Power Sources 115 (2003) 81.
[33] A.A. Shah, G.S. Kim, W. Gervais, A. Young, K. Promislow, J. Li, S. Ye, J. Power Sources 160 (2006) 1251.
[34] A.A. Shah, G.S. Kim, P.C. Sui, D. Harvey, J. Power Sources 163 (2007) 793.
[35] A.Z. Weber, J. Newman, J. Electrochem. Soc. 150 (2003) A1008.
[36] A.Z. Weber, J. Newman, J. Electrochem. Soc. 151 (2004) A311.
[37] I. Nazarov, K. Promislow, J. Electrochem. Soc. 154 (2007) B623.
[38] S. Motupally, A.J. Becker, J.W. Weidner, J. Electrochem. Soc. 147 (2000) 3171.
[39] J.P. Meyers, J. Newman, J. Electrochem. Soc. 149 (2002) A710.
[40] J.P. Meyers, J. Newman, J. Electrochem. Soc. 149 (2002) A718.
[41] J.P. Meyers, J. Newman, J. Electrochem. Soc. 149 (2002) A729.
[42] T. Schultz, K. Sundmacher, J. Power Sources 145 (2005) 435.
[43] W.P. Liu, C.Y. Wang, J. Power Sources 164 (2007) 189.
[44] V.A. Danilov, J. Lim, I. Moon, H. Chang, J. Power Sources 162 (2006) 992.
[45] J.H. Nam, M. Kaviany, Int. J. Heat Mass Transfer 46 (2003) 4595.
[46] U. Pasaogullary, C.Y. Wang, Electrochim. Acta 49 (2004) 4359.
[47] A.Z. Weber, J. Newman, J. Electrochem. Soc. 152 (2005) A677.
[48] J.T. Hinatsu, M. Mizuhata, H. Takenaka, J. Electrochem. Soc. 141 (1994) 1493.
[49] S.H. Ge, X.G. Li, B.L. Yi, I.M. Hsing, J. Electrochem. Soc. 152 (2005) A1157.